

**Modulated Self-Assembly of hcp Topology MOFs of Zr/Hf and the Extended 4,4'-
(Ethyne-1,2-diyl)dibenzoate Linker**

Sophia S. Boyadjieva,^a Francesca C. N. Firth,^b Mohammad R. Alizadeh Kiapi,^c David Fairen Jimenez,^c Sanliang Ling,^d Matthew J. Cliffe^{e*} and Ross Forgan^{a*}

^aWestCHEM School of Chemistry, University of Glasgow, Joseph Black Building, University Avenue, Glasgow G12 8QQ, UK. Email: ross.forgan@glasgow.ac.uk

^bYusuf Hamied Department of Chemistry, University of Cambridge, Cambridge CB2 1EW, UK.

^cThe Adsorption & Advanced Materials Laboratory (A2ML), Department of Chemical Engineering & Biotechnology, University of Cambridge, Philippa Fawcett Drive, Cambridge CB3 0AS, UK.

^dAdvanced Materials Research Group, Faculty of Engineering, University of Nottingham, University Park, Nottingham NG7 2RD, UK.

^eSchool of Chemistry, University of Nottingham, University Park, Nottingham, NG7 2RD, UK.
Email: matthew.cliffe@nottingham.ac.uk

SUPPORTING INFORMATION

Table of Contents

S1. General Experimental Remarks.	S3.
S2. Materials and Synthesis.	S4.
S2.1. Acetic Acid Modulation.	S4.
S2.2. Water Addition.	S4.
S2.3. Optimised Syntheses.	S7.
S3. Density Functional Theory.	S9.
S4. Pawley Refinement.	S10.
S5. Activation and Characterisation.	S11.
S6. BETSI Analysis	S26.
S7. GCMC Simulations	S21.
S8. Bromination Attempts.	S27.
S9. References.	S30.

S1. General Experimental Remarks

Chemicals: All chemicals and solvents were purchased from Alfa Aesar, Acros Organics, Fisher Scientific, Fluorochem, Sigma-Aldrich, Tokyo Chemical Industry and VWR and used without further purification.

Nuclear Magnetic Resonance (NMR): NMR spectra were recorded on either a Bruker AVIII 400 MHz spectrometer or a Bruker AVI 400 MHz Spectrometer and referenced to residual solvent peaks.

Powder X-ray Diffraction (PXRD): PXRD measurements were carried out at 298 K using a PANalytical X'Pert PRO diffractometer (λ (CuK α) = 1.54056 Å) on a mounted bracket sample stage. Data were collected over the range 3 – 45 °.

Thermal Gravimetric Analysis (TGA): Measurements were carried out using a TA Instruments Q500 Thermogravimetric Analyser. Measurements were collected from room temperature to 800 °C with a heating rate of 10 °C/min in air.

Infrared Spectroscopy (IR): Infrared spectra of solids were obtained via a Shimadzu Fourier Transform Infrared Spectrometer, FTIR-8400S, fitted with a Diamond ATR unit.

Scanning Electron Microscopy (SEM): The powder samples were coated with Pd for 50 seconds using Polaron SC7640 sputter coater and imaged using a Carl Zeiss Sigma Variable Pressure Analytical SEM with Oxford Microanalysis.

Gas Uptake: N₂ adsorption isotherms were carried out at 77 K on a Quantachrome Autosorb iQ gas sorption analyser. Samples were degassed under vacuum at 120 °C for 20 hours using the internal turbo pump. BET surface areas were calculated from the isotherms using the Micropore BET Assistant in the Quantachrome ASiQwin operating software.

Pore-Size Distribution: Pore size distributions were calculated using the N₂ at 77 K on carbon (slit pore, QSDFT, equilibrium model) calculation model within the Quantachrome ASiQwin operating software.

S2. Materials and Synthesis

The ligand, 4,4'-(ethyne-1,2-diyl)dibenzoic acid (EDB-H₂) was synthesised according to a modified literature procedure.^{S1, S2}

S2.1. Acetic Acid Modulation

During synthetic optimisations, the quantities of both acetic acid and water were varied in attempts to determine the structure-directing role of each modulating agent, particularly as water has been proposed to play a major role in phase selection.^{S3} When keeping the water concentration in the synthesis constant, variation of acetic acid content (Figure S1) mostly resulted in highly crystalline materials of the **hcp** phase, although the reaction between HfCl₄ and EDB-H₂ in the presence of only 100 equiv. of acetic acid gave an unknown phase.

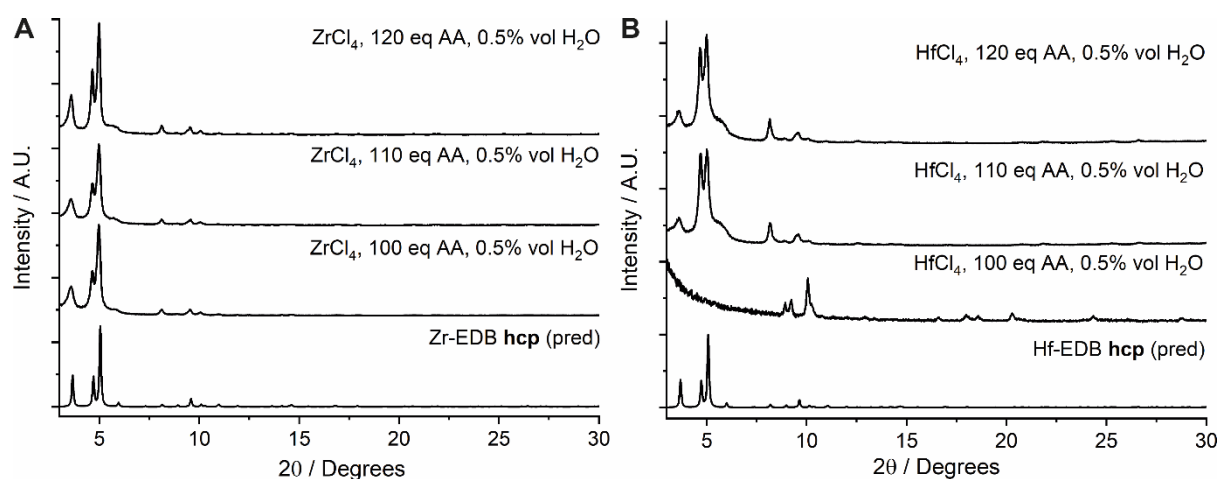


Figure S1. Stacked powder X-ray diffractograms of MOF samples prepared with (A) ZrCl₄, or (B) HfCl₄, alongside EDB-H₂, 0.5% (v/v) water, and varying quantities of acetic acid (AA) in DMF at 150 °C. Comparison is made with predicted patterns for the **hcp** phase MOF derived from DFT models (see Section S3).

S2.2. Water Addition

The water content was increased to determine its potential role in the formation of the nanosheet topology (**hns**) material,^{S3} however even at the highest concentrations of added

water, both the Zr- and Hf-EDB samples exhibited powder X-ray diffractograms consistent with the **hcp** phase (Figure S2).

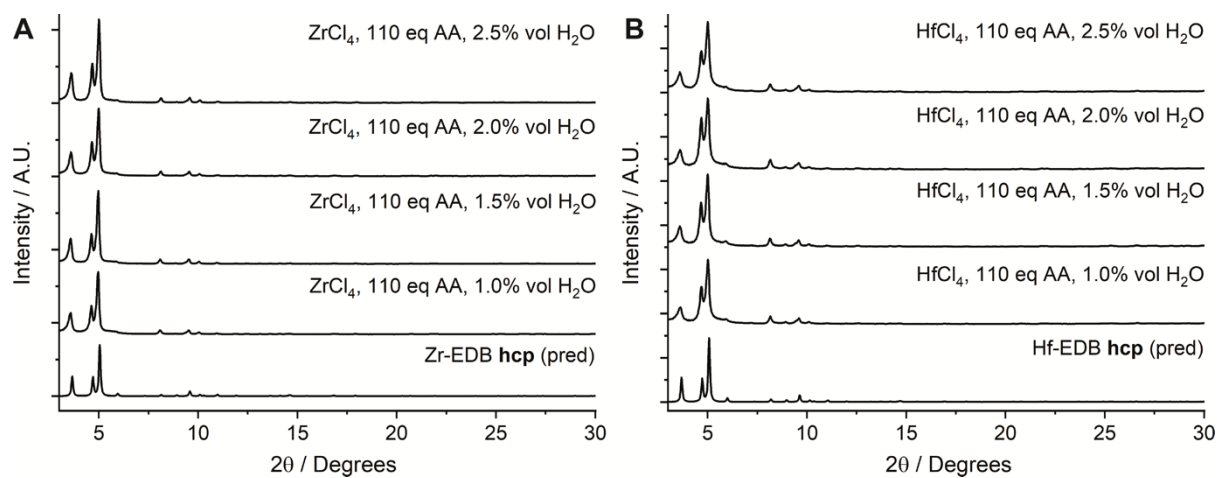


Figure S2. Stacked powder X-ray diffractograms of MOF samples prepared with (A) ZrCl₄, or (B) HfCl₄, alongside EDB-H₂, 110 equivalents of acetic acid (AA), and varying quantities of water in DMF at 150 °C. Comparison is made with predicted patterns for the **hcp** phase MOF derived from DFT models (see Section S3).

SEM images of the Zr-EDB (Figure S3) and Hf-EDB (Figure S4) samples synthesised with varying water contents show the desert rose formations characteristic of the **hcp** phase.^{S1}

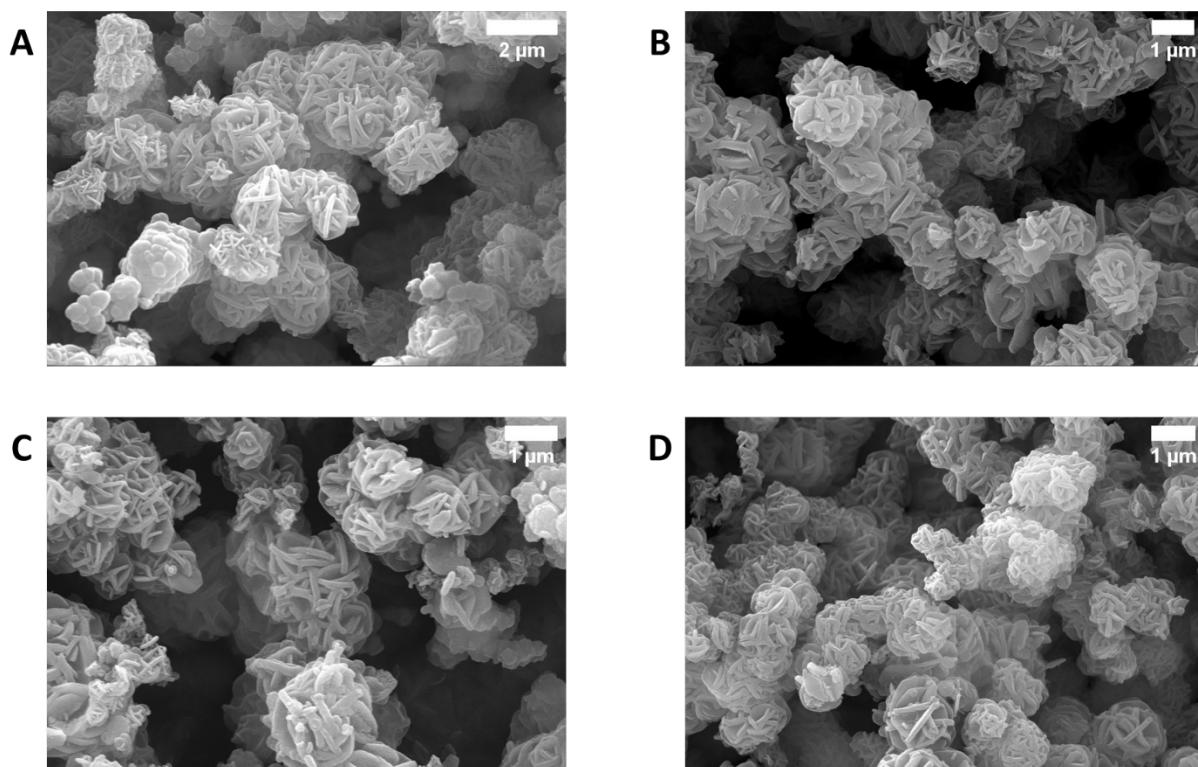


Figure S3. SEM images of the Zr-EDB MOF synthesised using (A) 1%, (B) 1.5%, (C) 2%, and (D) 2.5% vol. of water.

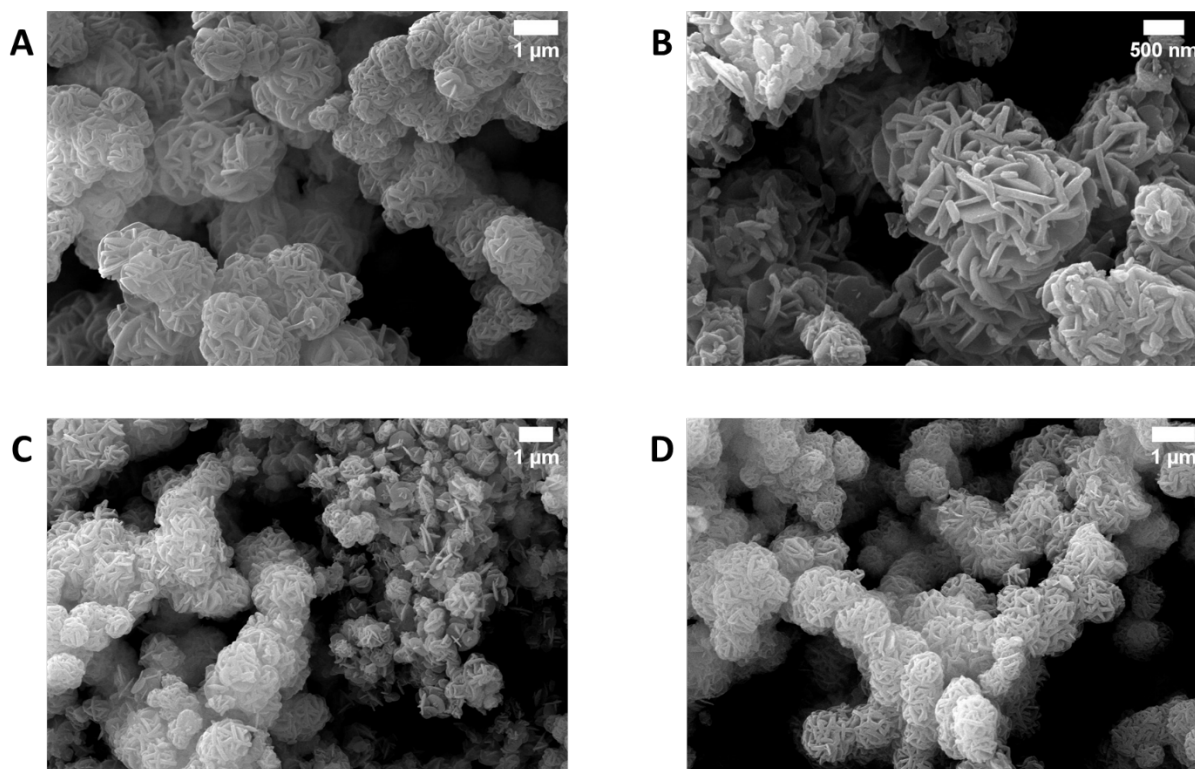


Figure S4. SEM images of the Hf-EDB MOF synthesised with (A) 1%, (B) 1.5%, (C) 2%, and (D) 2.5% vol. of water.

S2.3. Optimised Syntheses

Optimised Synthesis of GUF-12(Zr)

ZrCl₄ (0.078 g, 0.3375 mmol, 1 eq.) and alkyne ligand (0.090 g, 0.3375 mmol, 1 eq.) were suspended in DMF (10 ml) via sonication in a glass jar and were subsequently transferred to a Teflon vessel with the aid of DMF (5 ml). H₂O (0.075 ml, 0.5% vol. and acetic acid (2.124 ml, 37.125 mmol, 110 eq.) were added and the Teflon vessel was put in a metal autoclave and left in oven (150 °C) overnight. Reaction was then cooled down to room temperature and the MOF was centrifuged (4500 rpm, 15 min), washed with fresh DMF (2 x 15 ml), acetone (3 x 15 ml), and left drying in desiccator. Product was collected as a peachy coloured powder and analysed by powder X-ray diffraction to confirm phase purity (Figure S5A).

Optimised Synthesis of GUF-12(Hf)

HfCl₄ (0.108 g, 0.3375 mmol, 1 eq.) and alkyne ligand (0.090 g, 0.3375 mmol, 1 eq.) were suspended in DMF (10 ml) via sonication in a glass jar and were subsequently transferred to a

Teflon vessel with the aid of DMF (5 ml). H₂O (0.075 ml, 0.5% vol. and acetic acid (2.124 ml, 37.125 mmol, 110 eq.) were added and the Teflon vessel was put in a metal autoclave and left in oven (150 °C) overnight. Reaction was then cooled down to room temperature and the MOF was centrifuged (4500 rpm, 15 min), washed with fresh DMF (2 x 15 ml), acetone (3 x 15 ml), and left drying in desiccator. Product was collected as a peachy coloured powder and analysed by powder X-ray diffraction to confirm phase purity (Figure S5B).

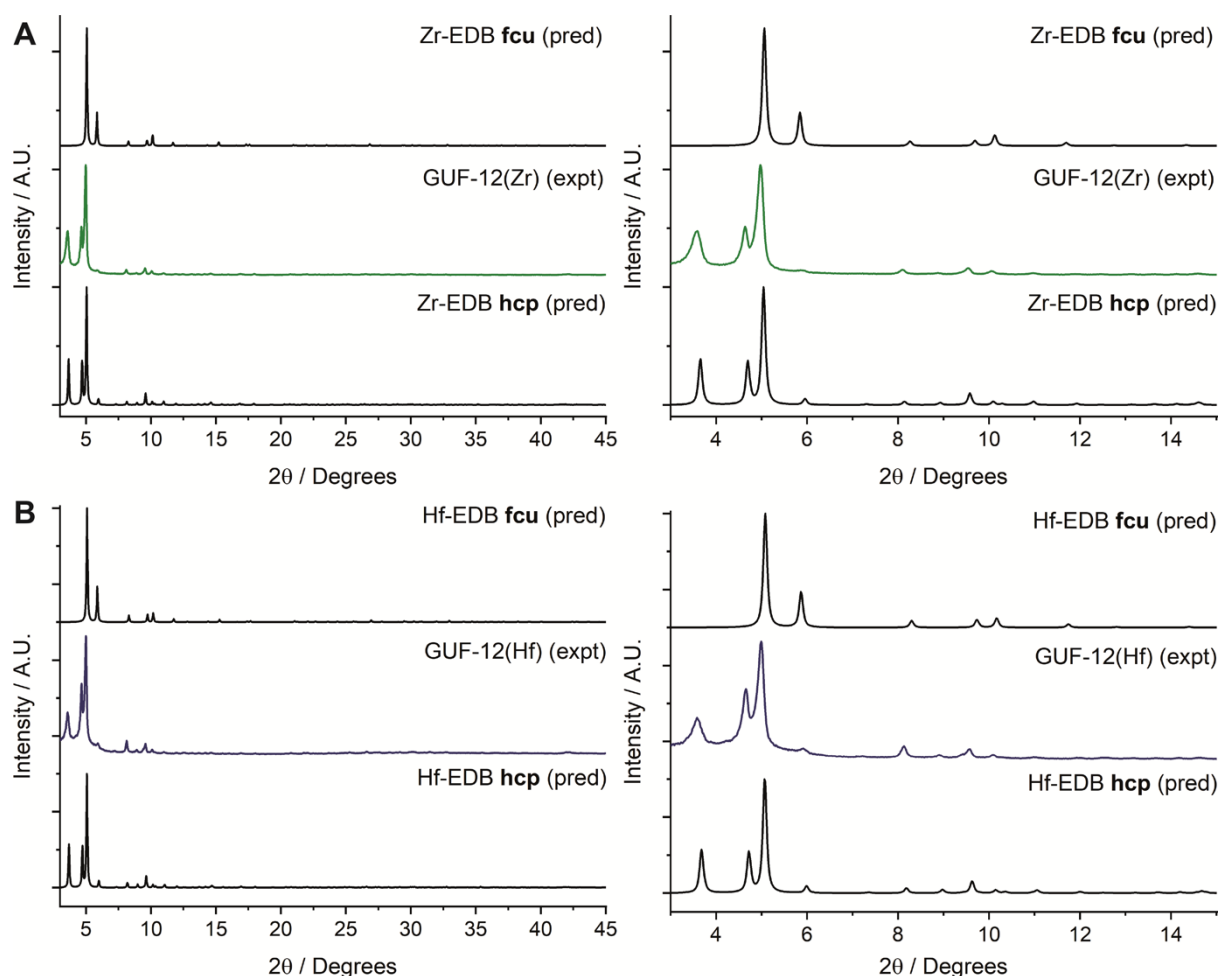


Figure S5. Stacked powder X-ray diffractograms of (A) GUF-12(Zr) and (B) GUF-12(Hf), compared with made with predicted patterns for the **hcp** phase MOFs derived from DFT models (see Section S3) and the **fcu** phase MOFs derived from their crystal structures.^{S1} Further characterisation is provided in Figures 2-4 of the manuscript.

S3. Density Functional Theory

Structural model of the **hcp** topology phases containing Zr/Hf and EDB²⁻ were manually generated to allow comparison with experimental diffraction data (Figure S6). Density functional theory (DFT) calculations were used to relax both structures. All DFT calculations were performed using the CP2K code, which uses a mixed Gaussian/plane-wave basis set.^{S4, S5} Double- ζ polarization quality Gaussian basis sets^{S6} and a 600 Ry plane-wave cutoff for the auxiliary grid were employed in conjunction with the Goedecker-Teter-Hutter pseudopotentials.^{S7, S8} All DFT calculations were performed in the Γ -point approximation with a sufficiently large cell (a total of 600 atoms per cell). Total energy calculations and structural optimizations, including both atomic coordinates and cell parameters, were performed under periodic boundary conditions at the DFT level using the PBE exchange and correlation functional,^{S9} with Grimme's D3 van der Waals correction (PBE+D3).^{S10} A convergence threshold of 1.0×10^{-8} Hartree was used for the self-consistent field cycle, and structural optimizations were considered to have converged when the maximum force on all atoms falls below 1.0×10^{-4} Hartree/Bohr.

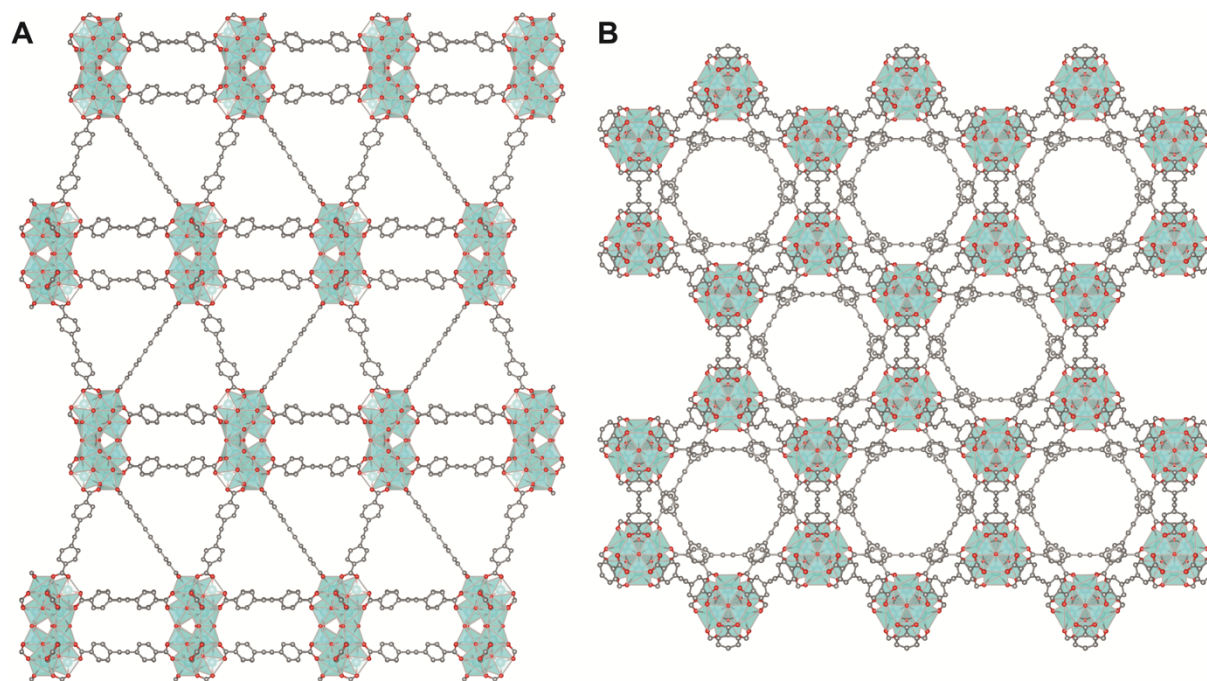


Figure S6. Images of the DFT structural model of GUF-12(Zr) viewed along (A) the crystallographic *a* axis and (B) the crystallographic *c* axis. H atoms omitted for clarity.

S4. Pawley Refinement

Pawley refinement of the experimental powder X-ray diffraction data was carried out in space group $P6_3/mmc$ using Topas Academic version 6.^{S11} The background was modelled using a freely refining Chebyshev polynomial with 9 parameters and a broad Gaussian peak (FWHM ca. 3°) centered at ca. 3° , and a sample-height correction was also refined. The refined parameters were for Zr: $a = 21.612(3)$, $c = 48.014(12)$ with $R_{wp} = 5.009$, GoF = 5.362; and for Hf: $a = 21.535(3)$, $c = 47.869(14)$ with $R_{wp} = 4.878$, GoF = 5.345.

S5. Activation and Characterisation

As-synthesised samples of GUF-12(Zr) and GUF-12(Hf) were activated by heating at 120 °C for 20 h under turbopump vacuum to remove residual solvents.

PXRD patterns of the samples were taken after activation to determine if any changes had occurred. The as-synthesised samples were dried in a desiccator prior to all analysis, and a smaller region of the patterns is displayed to be able to observe the shifts more clearly (Figure S7). No major changes are observed for either GUF-12(Zr) or GUF-12(Hf) other than the relative intensities of certain reflections.

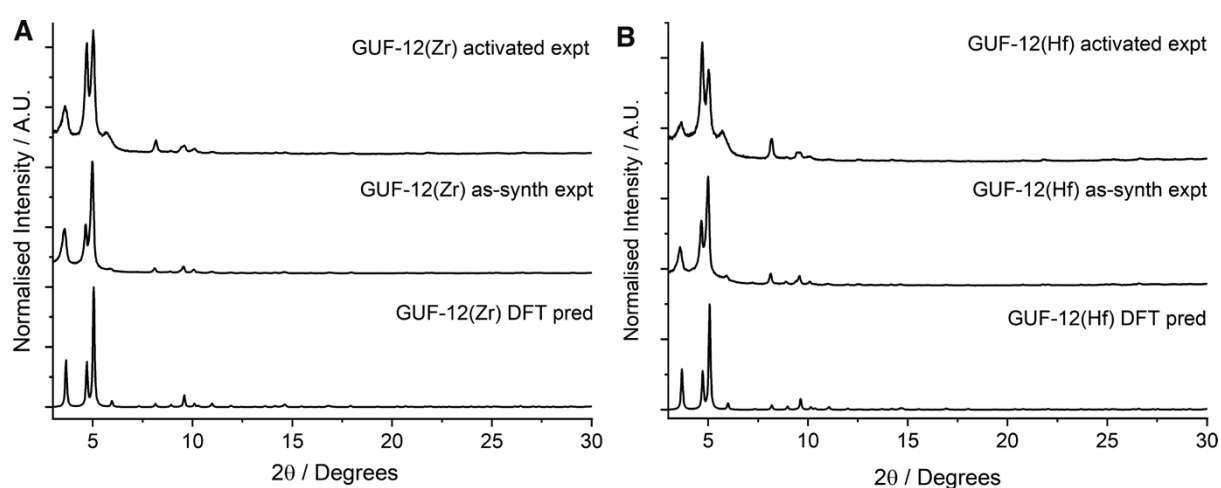


Figure S7. PXRD patterns of as-synthesised and activated samples of (A) GUF-12(Zr) and (B) GUF-12(Hf) compared to PXRD patterns predicted from their respective DFT model structures (Section S3).

The slight differences exhibited in the PXRD patterns of the materials were further investigated by SEM (Figure S8). There was no significant change comparing the samples before and after activation.

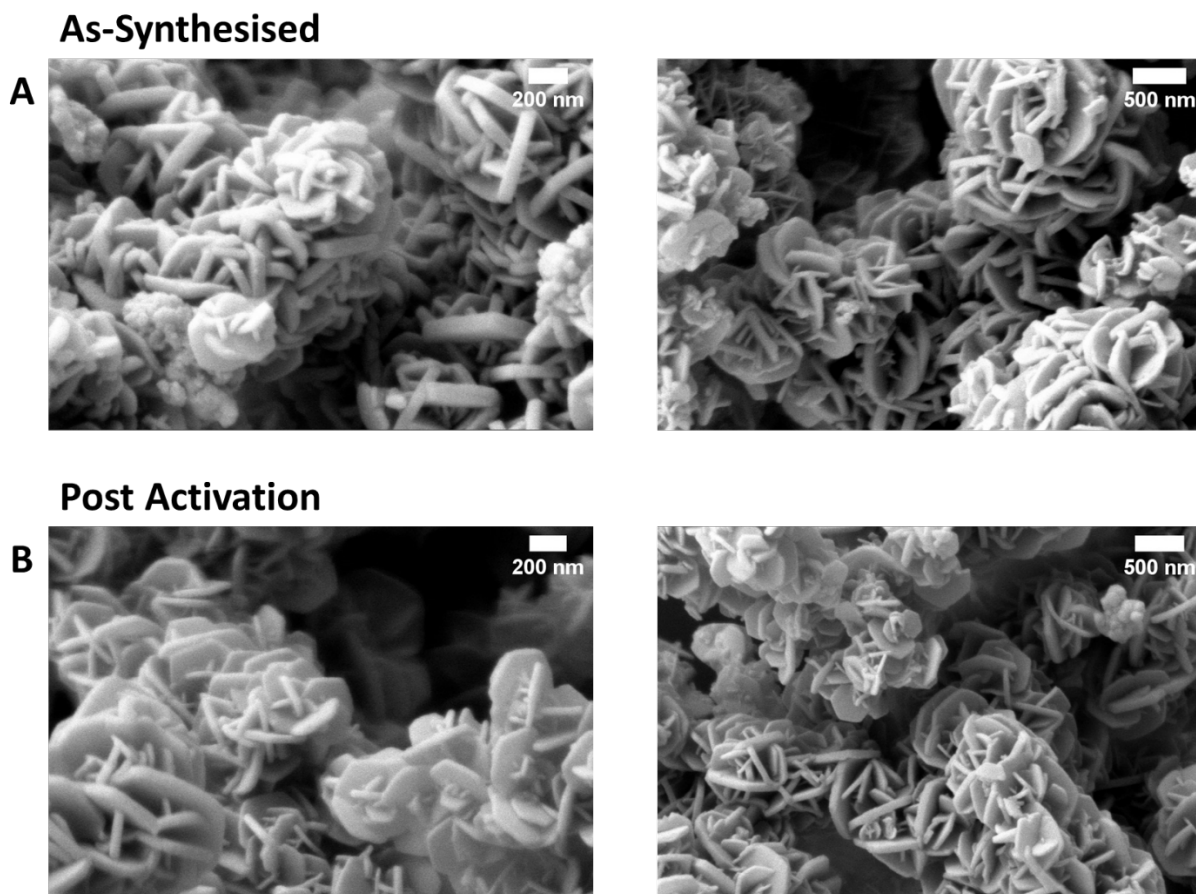


Figure S8. SEM images of (A) as-synthesised samples of GUF-12(Zr) (left) and GUF-12(Hf) (right) compared to (B) activated samples of GUF-12(Zr) (left) and GUF-12(Hf) (right).

IR spectroscopic data of the three frameworks was collected before and after BET activation (Figure S9). No significant change was observed for either of the MOFs.

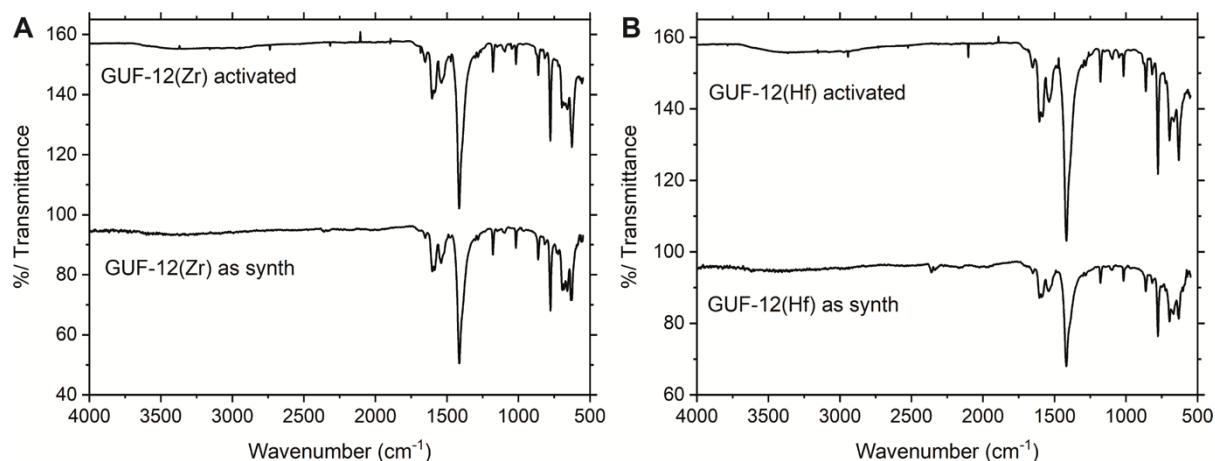


Figure S9. IR spectra of as synthesised and activated samples of (A) GUF-12(Zr) and (B) GUF-12(Hf).

¹H NMR spectroscopy was applied to assess the composition of the activated MOFs. All samples were acid digested (D₂SO₄/DMSO-*d*₆) as MOFs cannot be dissolved in a deuterated solvent and need to be broken down as to analyse. For both GUF-12(Zr) (Figure S10) and GUF-12(Hf) (Figure S11), a resonance assigned to the protons of the acetate methyl group is visible at 1.8 ppm, suggesting the incorporation of the modulator within the frameworks as defects. Integral ratios were used to determine the content of acetate in the MOFs, yielding acetate:linker ratios of 1:3.3 for GUF-12(Zr) and 1:2.5 for GUF-12(Hf). No significant change was observed in the acetate presence in the post BET activation samples, further suggesting that for both MOFs, acetate capping within the structure occurs i.e. acetate coordinates at clusters as defects. No formate originating from DMF decomposition is present, likely due to the large excess of acetic acid present in the syntheses.

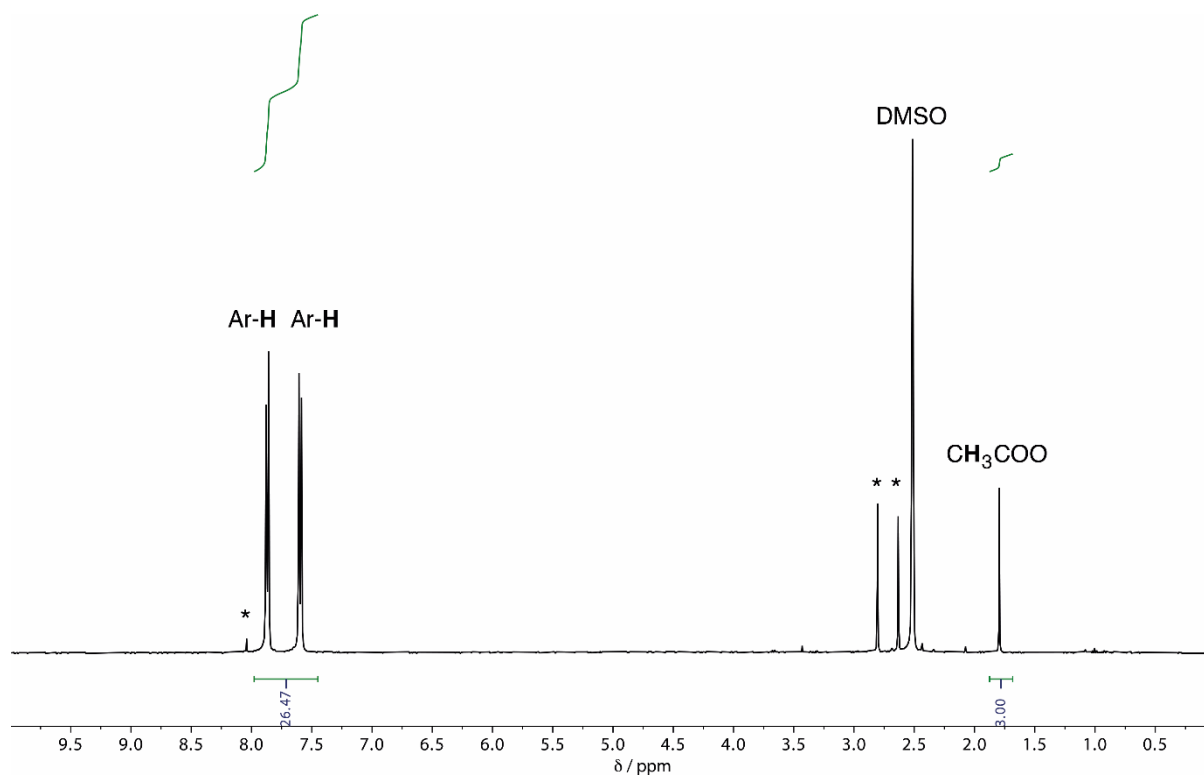


Figure S10. Excerpt of ^1H NMR spectrum ($\text{DMSO-}d_6 / \text{D}_2\text{SO}_4$) of activated GUF-12(Zr). The ratio of the integration of the resonances assigned to the acetate methyl group to the aromatic protons of the EDB^{2-} linker is 3:26.47. Given there are eight aromatic protons on each EDB^{2-} linker, this gives an acetate to linker ratio of 1:3.3. The resonances marked with an asterisk (*) at $\delta = 2.6, 2.8,$ and 8 ppm are assigned to DMF protons. These were present in varying ratios across samples (including increasing after activation) suggesting that they are a contaminant in the NMR tubes.

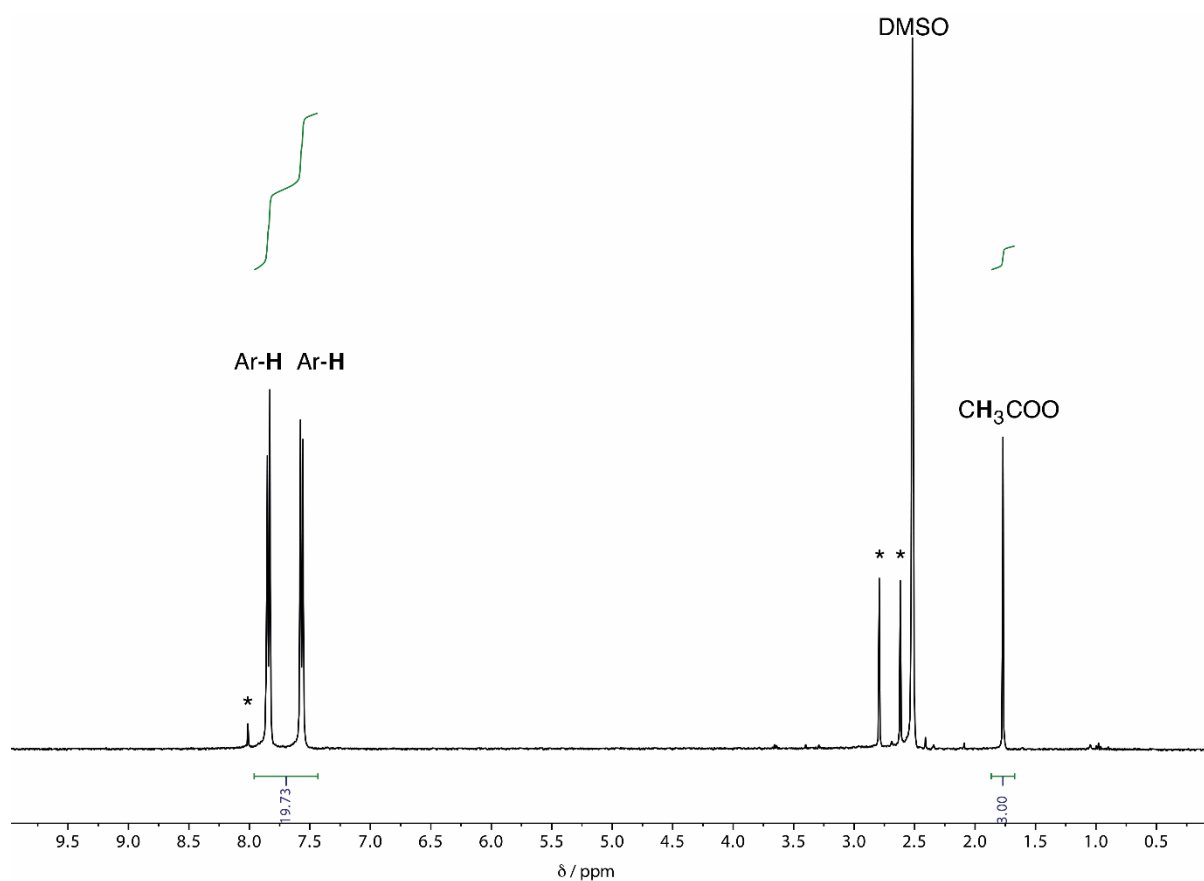


Figure S11. Excerpt of ^1H NMR spectrum ($\text{DMSO-}d_6 / \text{D}_2\text{SO}_4$) of activated GUF-12(Zr). The ratio of the integration of the resonances assigned to the acetate methyl group to the aromatic protons of the EDB^{2-} linker is 3:19.73. Given there are eight aromatic protons on each EDB^{2-} linker, this gives an acetate to linker ratio of 1:2.5. The resonances marked with an asterisk (*) at $\delta = 2.6, 2.8,$ and 8 ppm are assigned to DMF protons. These were present in varying ratios across samples (including increasing after activation) suggesting that they are a contaminant in the NMR tubes.

S6. BETSI Analysis

The BET areas of the two MOFs were calculated from the experimental N₂ adsorption isotherms using BETSI, a publicly available software package that fully implements the extended Rouquerol criteria for an unambiguous BET area assignment.^{S12} For calculations, all four criteria and a minimum number of point equal to three are considered. The analysis is presented in Figures S12-S15.

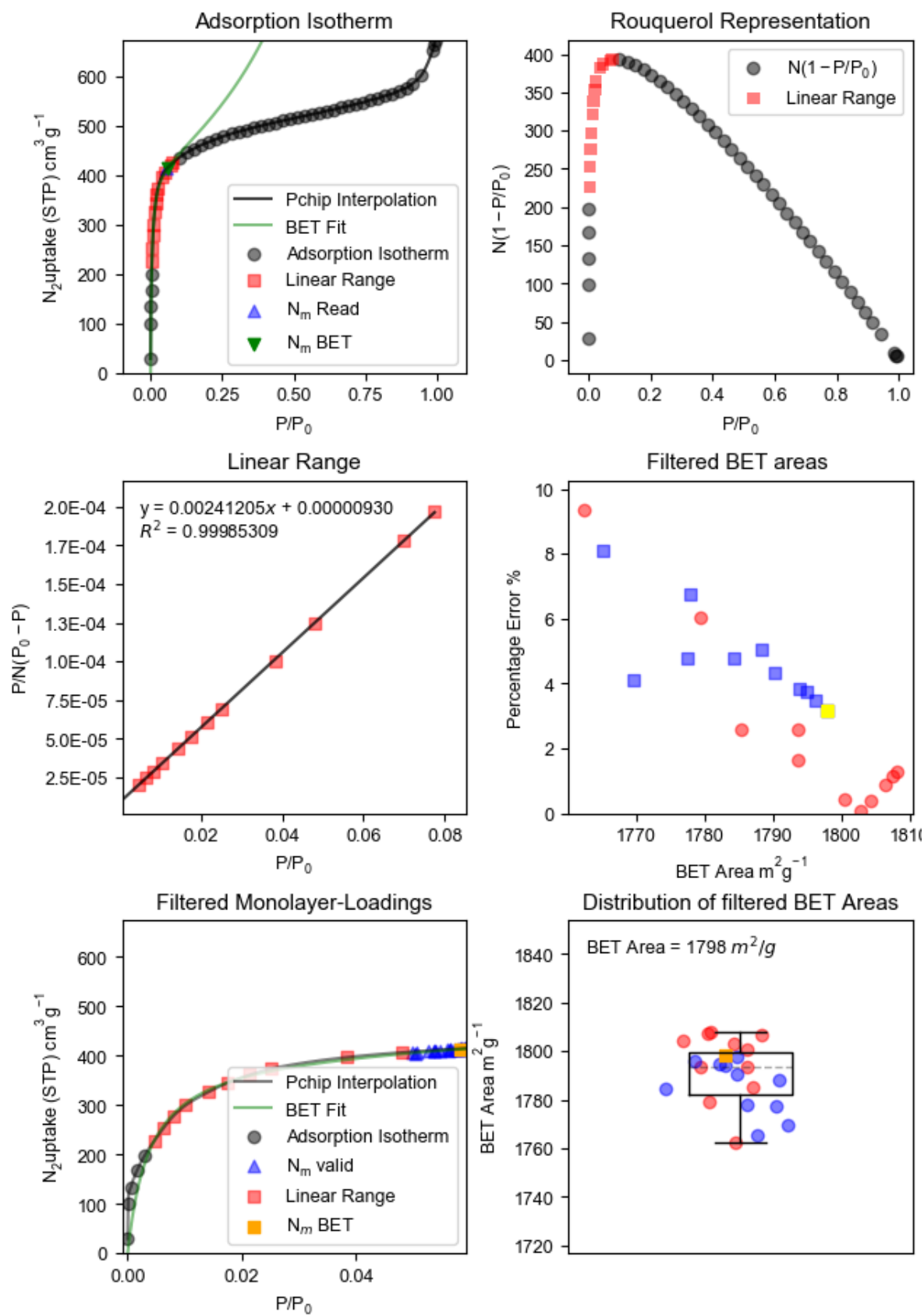


Figure S12. BETSI analysis of GUF-12(Zr) from the experimental N_2 adsorption isotherm.

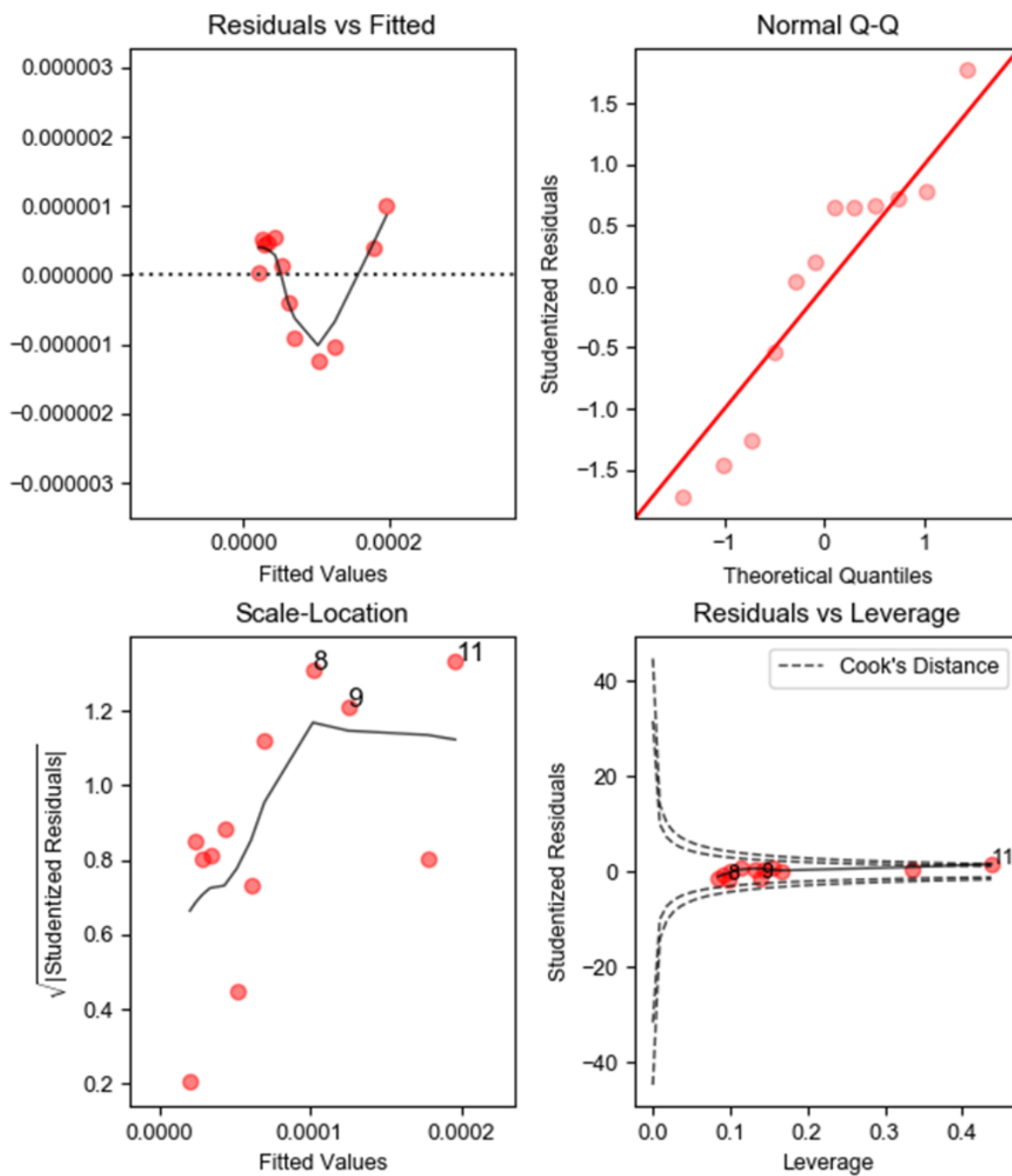


Figure S13. BETSI regression diagnostics for GUF-12(Zr) from the experimental N_2 adsorption isotherm.

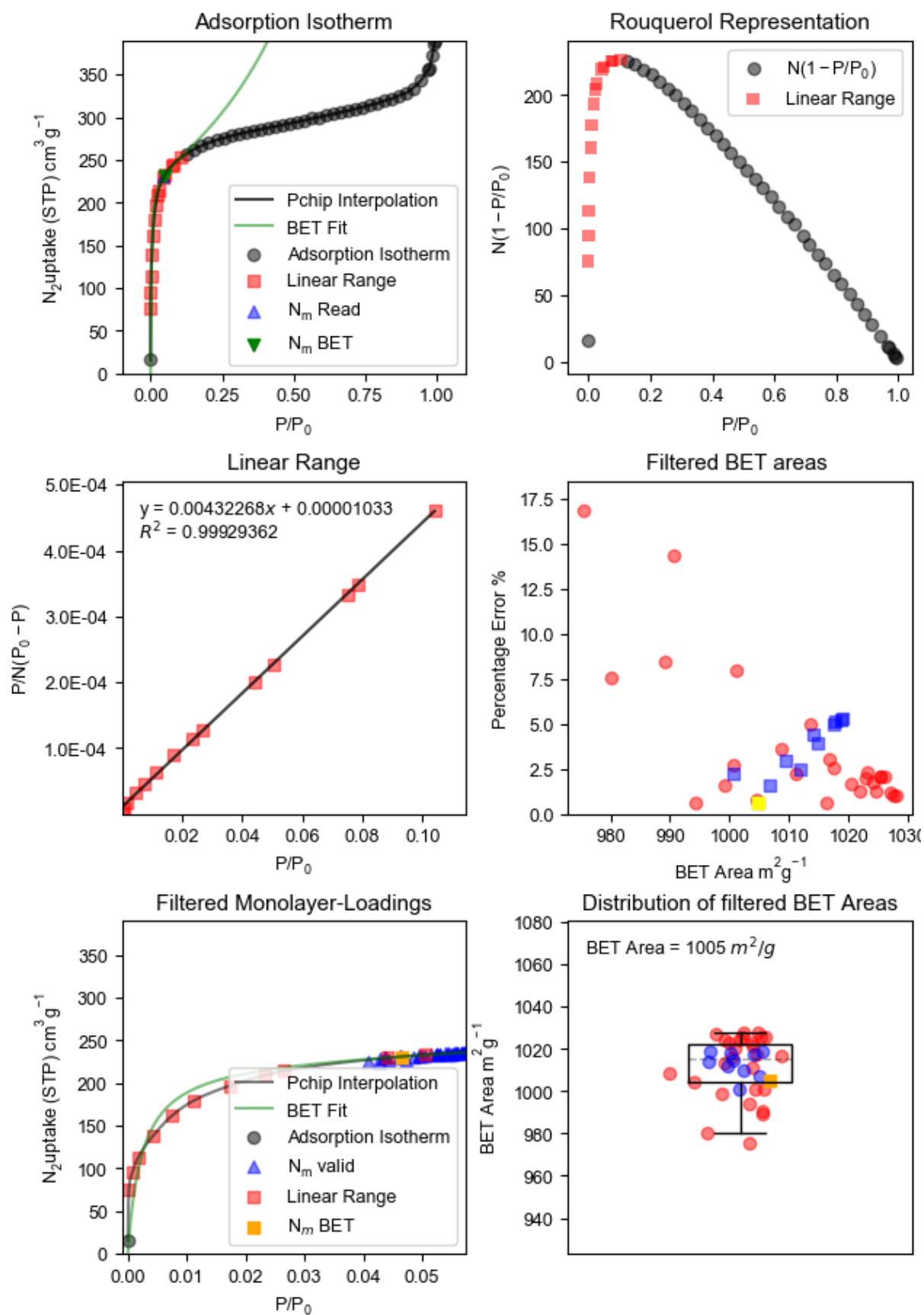


Figure S14. BETSI analysis of GUF-12(Hf) from the experimental N_2 adsorption isotherm.

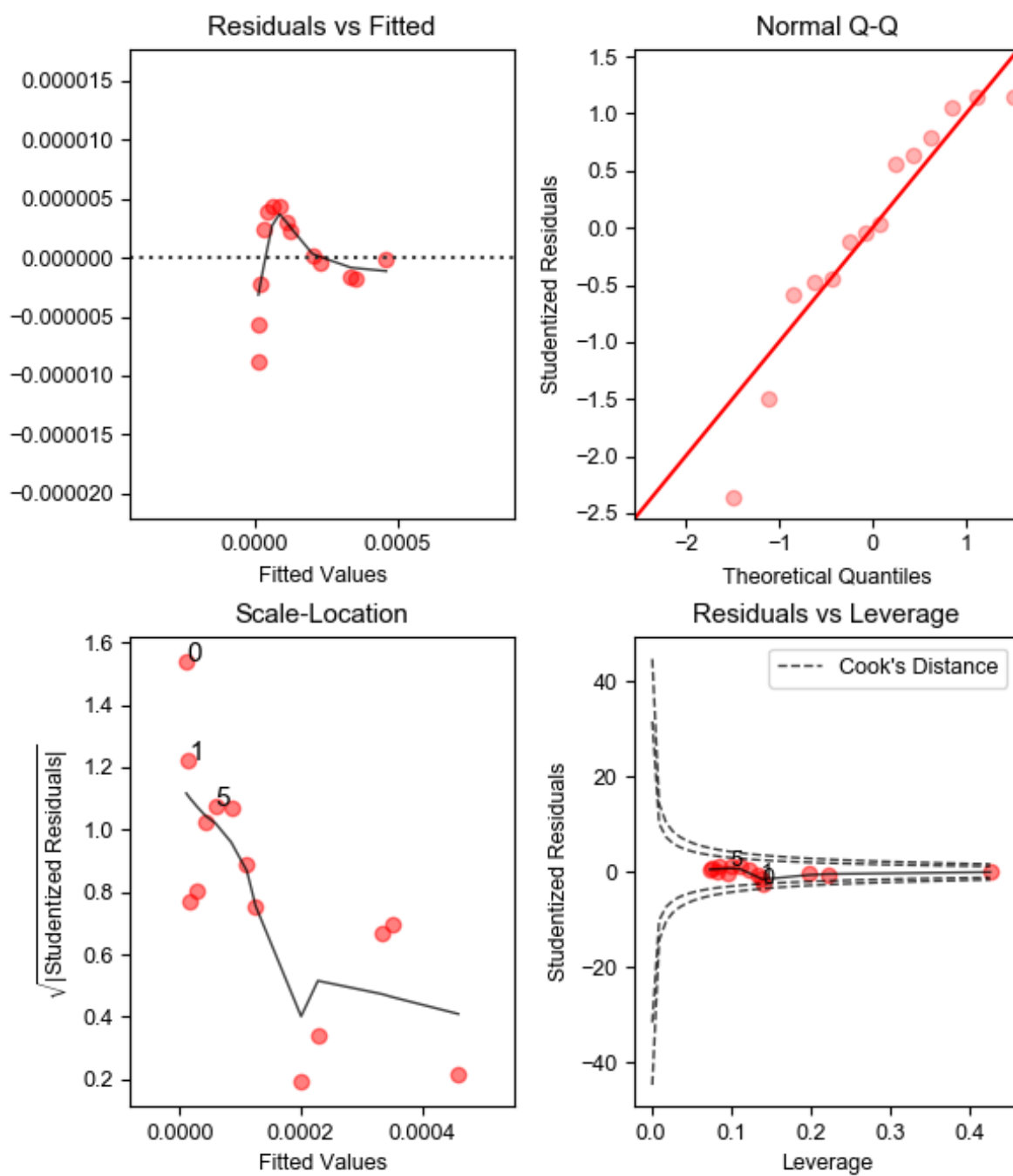


Figure S15. BETSI regression diagnostics for GUF-12(Hf) from the experimental N₂ adsorption isotherm.

S7. GCMC Simulations

All Grand Canonical Monte Carlo (GCMC) simulations were conducted using the RASPA molecular simulation software.^{S13} GCMC simulations of N₂ adsorption on the DFT model structures of GUF-12(Zr) and GUF-12(Hf) were performed at 77 K and at several different pressure values between 1×10^{-7} and 1 bar. Rigid frameworks were considered for the structures meaning all their atom positions were kept fixed during the simulations. The Lennard–Jones (LJ) potential was used to model the interactions between the framework and gas atoms with a cut-off value of 12.8 Å, beyond which the interactions were neglected. In turn, the size of the simulation box is defined large enough, equal to $2 \times 2 \times 1$ of the frameworks' unit cells, so that the length is larger than twice the cut-off range in all three dimensions. Besides, a Coulombic potential was also considered for nitrogen-nitrogen interactions. The LJ parameters for the framework atoms were taken from the DREIDING Force Field (DFF)^{S14} and, if not present there, from the Universal Force Field (UFF)^{S15} while for N₂, the parameters were obtained from the TraPPE force field.^{S16} To calculate gas-solid LJ parameters, Lorentz–Berthelot mixing rules were employed. Monte Carlo moves attempted in our simulations were insertions, deletions, translations, and rotation. For all pressure points, we used 10,000 cycles for equilibration followed by 20,000 cycles to calculate the ensemble averages. A cycle here is defined as the maximum of 20 or the number of molecules in the simulation cell. In order to convert pressure to fugacity, which is required for GCMC calculations, the Peng-Robinson equation of state was employed.

The simulated isotherms are compared to the experimental ones in Figure S16. It is clear that the simulations show a larger uptake, as they are based on a perfect crystalline material, whilst the experimental isotherms are susceptible to issues like pore blocking or minor amorphization. The simulated isotherms predict the overall shape of the experimental isotherms well, as seen in the logarithmic plots., indicating they are a good representation of the structure.

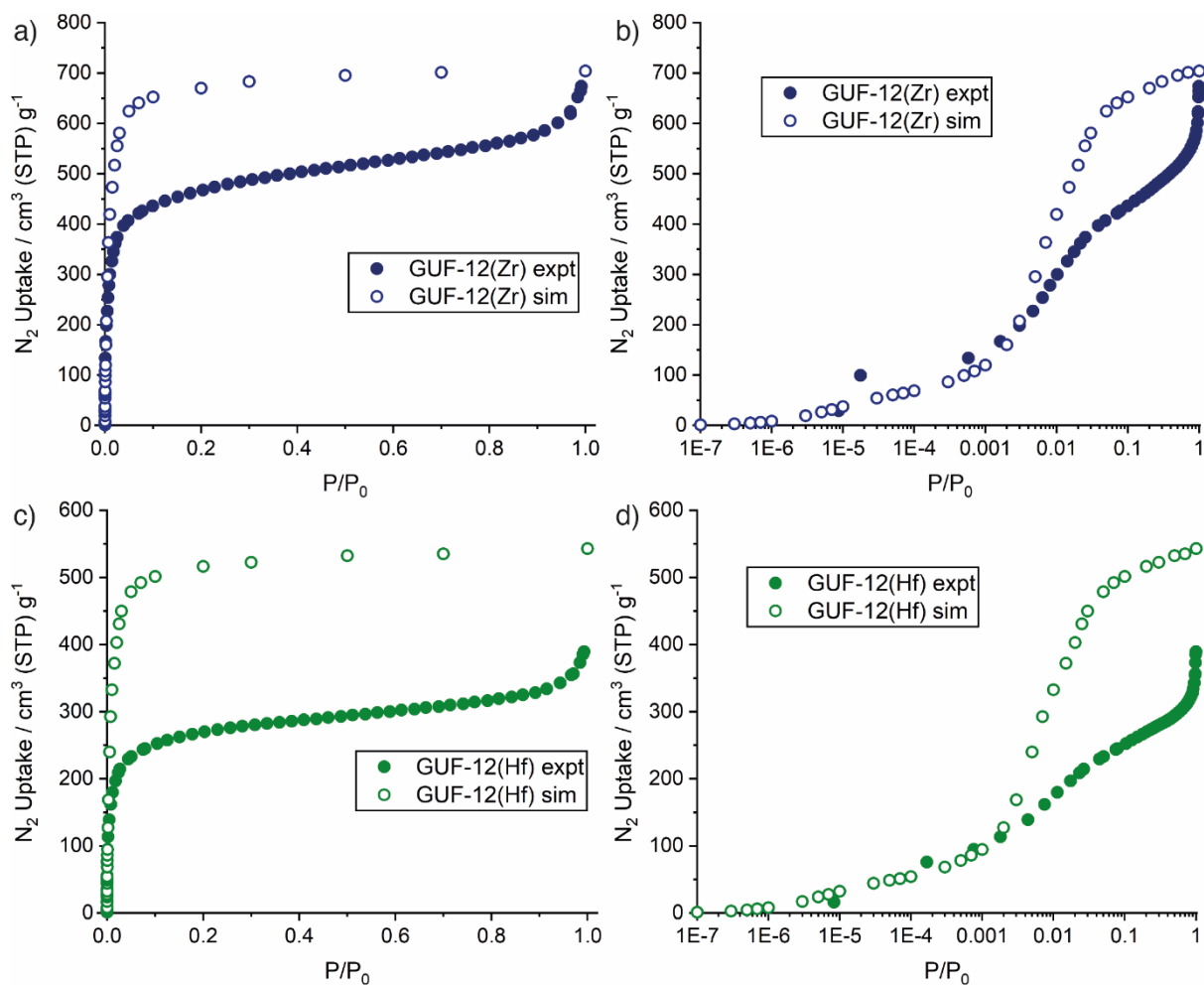


Figure S16. Comparison of simulated and experimental nitrogen adsorption isotherms for GUF-12(Zr) plotted with pressure on a) a linear scale and b) a logarithmic scale, and for GUF-12 (Hf) plotted with pressure on c) a linear scale and d) a logarithmic scale.

BETSI analysis^{S12} was used to determine the BET areas from the simulated N_2 adsorption isotherms (Figures S17-S20). These are compared with the experimental BET areas in Table S1.

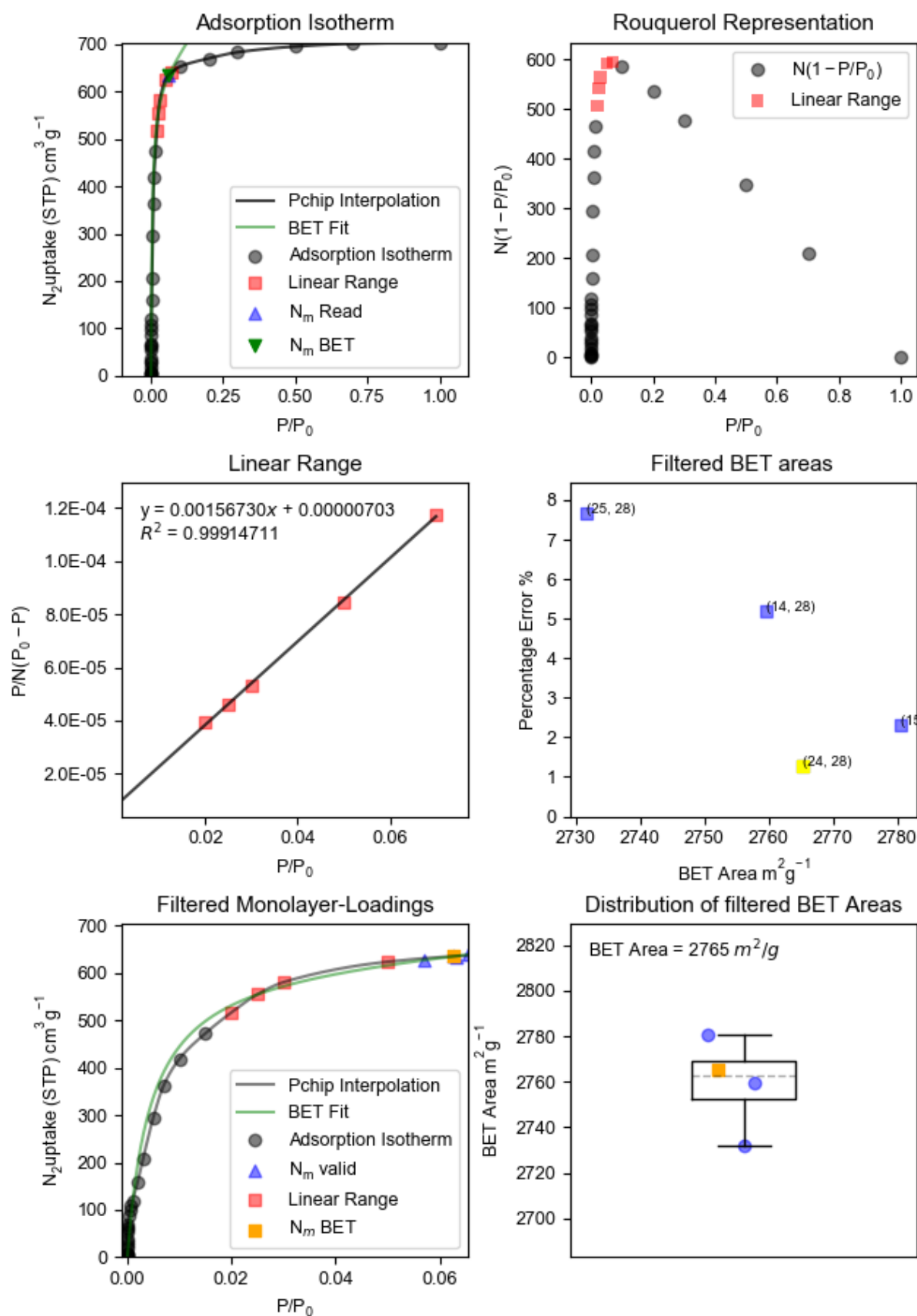


Figure S17. BETSI analysis of GUF-12(Zr) from the simulated N_2 adsorption isotherm.

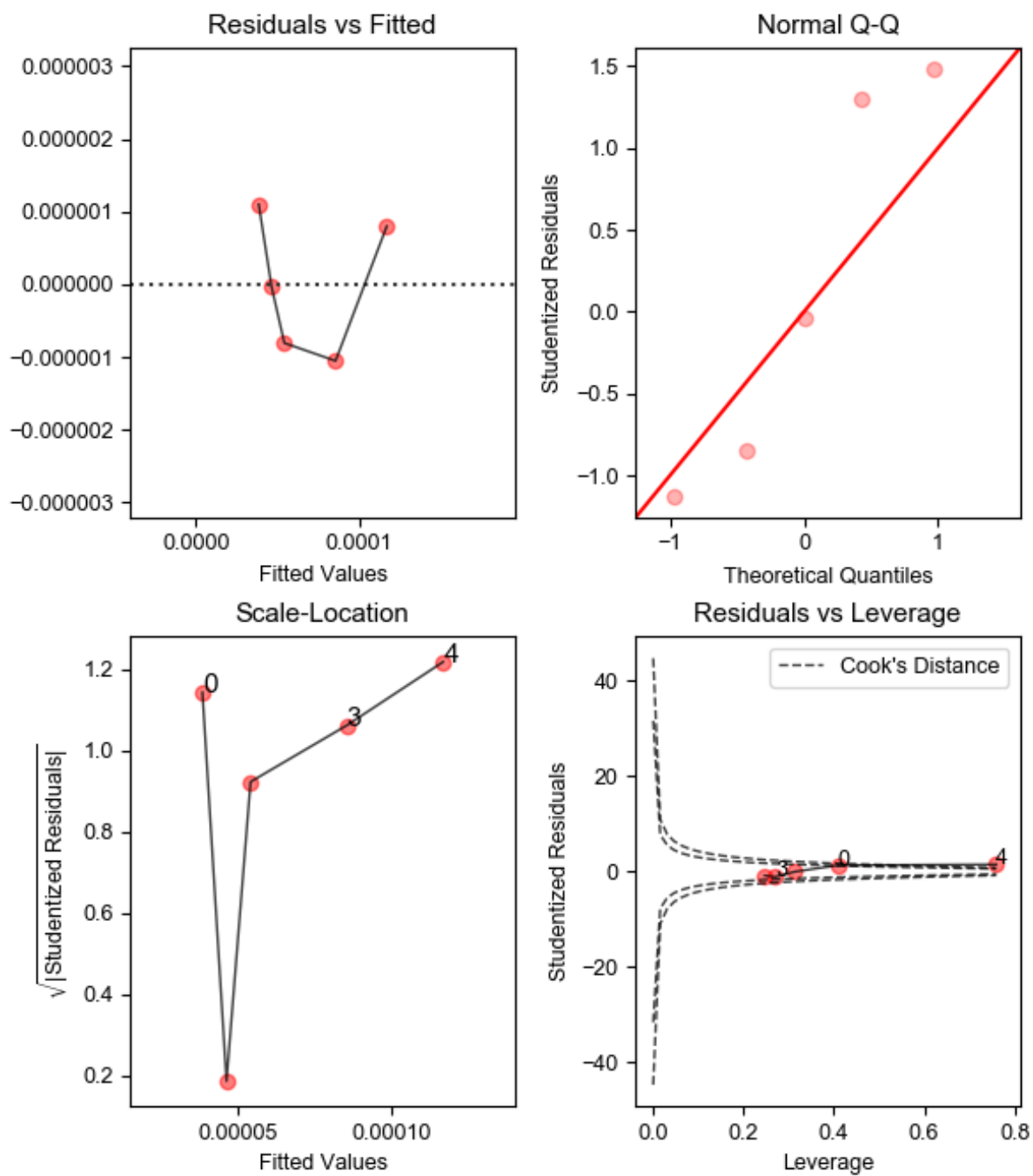


Figure S18. BETSI regression diagnostics for GUF-12(Zr) from the simulated N_2 adsorption isotherm.

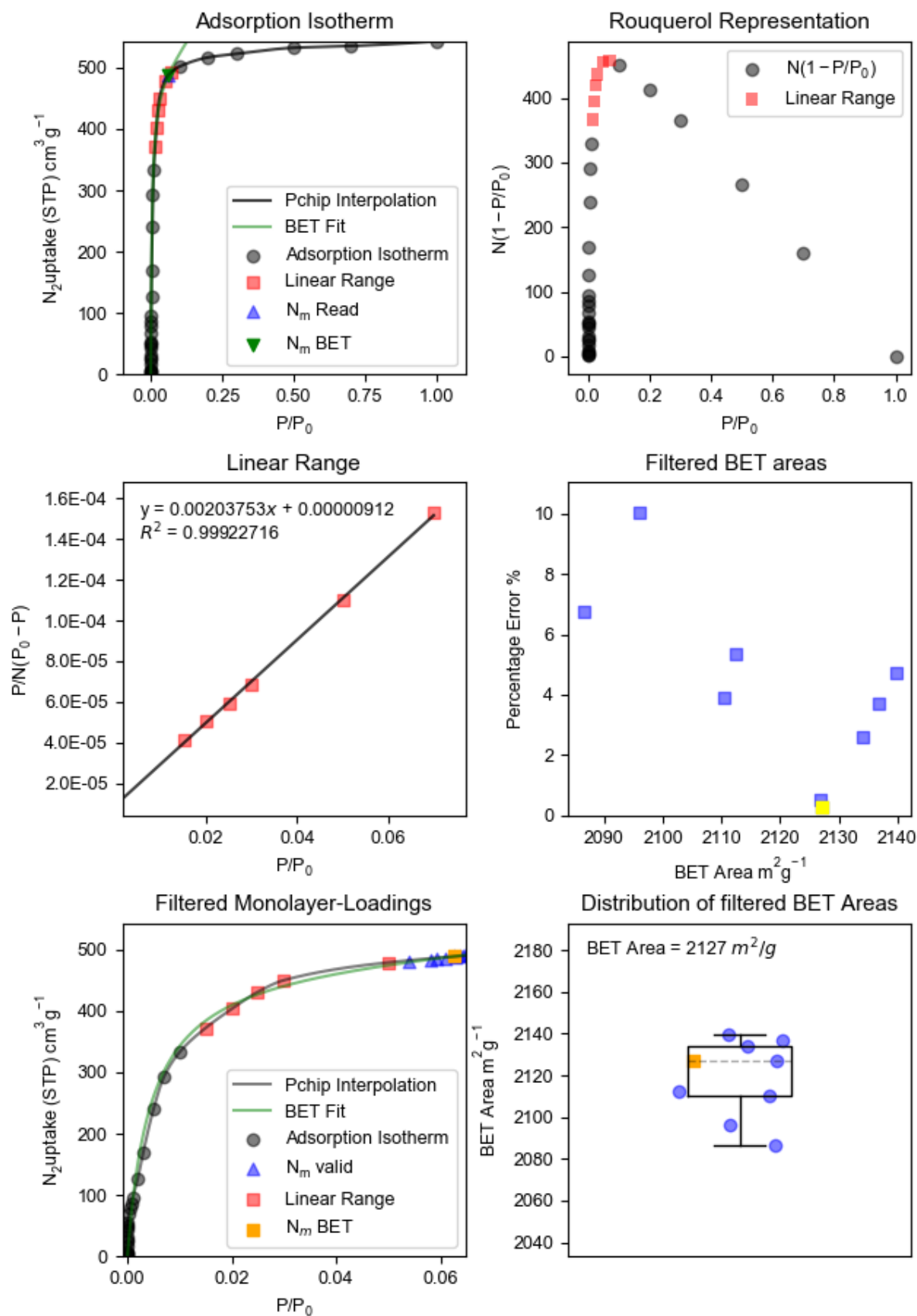


Figure S19. BETSI analysis of GUF-12(Hf) from the simulated N_2 adsorption isotherm.

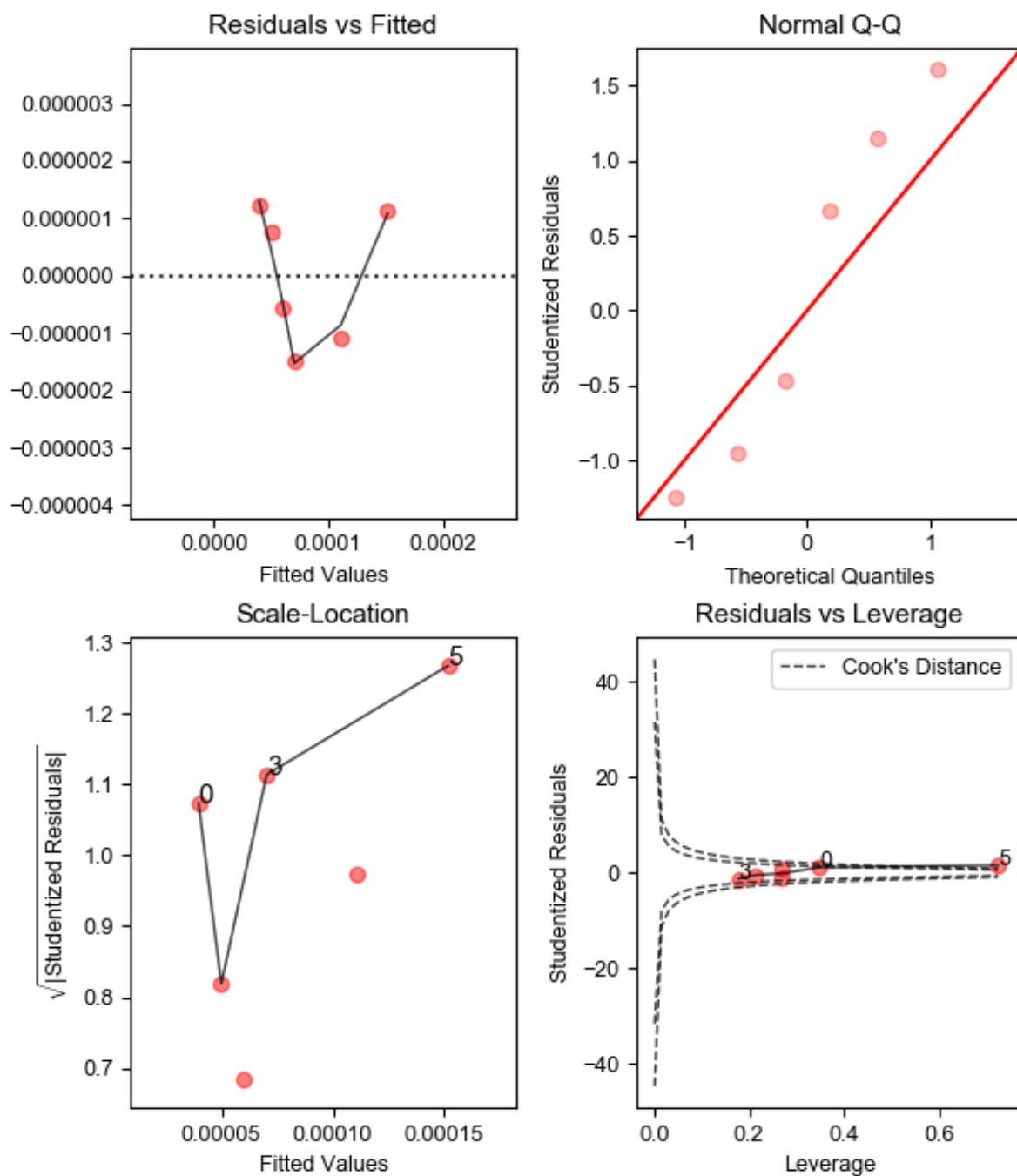


Figure S20. BETSI regression diagnostics for GUF-12(Hf) from the simulated N_2 adsorption isotherm.

Table S1. Comparison of BETSI calculated BET areas.

BETSI Area	Experiment	Simulation
GUF-12(Zr)	1798 $m^2 g^{-1}$	2765 $m^2 g^{-1}$
GUF-12(Hf)	1005 $m^2 g^{-1}$	2127 $m^2 g^{-1}$

S8. Bromination Attempts

Attempts to brominate the GUF-12 MOFs followed our published procedure that allowed successful brominating of the **fcu** analogues.^{S1} General bromination procedure:

GUF-12(Zr) (0.060 g) was suspended in chloroform (10 ml) and left overnight. After 24 h, the solvent was exchanged with fresh chloroform (10 ml) and bromine (0.265 ml, 5.15 mmol triple bond, 30 eq.) was added, vial was par filmed and left in the dark for 72 h. MOF was centrifuged (4500 rpm, 5 min), washed with fresh chloroform until washings were clear, and left drying in desiccator. Product was collected as a peachy coloured powder.

As with our previous reports,^{S1} the extent of bromination of the EDB²⁻ ligands was ascertained by ¹H NMR spectroscopy of acid-digested samples, whilst the retention of crystallinity (and thus stability) was assessed by powder X-ray diffraction. The results of the bromination of both GUF-12(Zr) and GUF-12(Hf) were variable, and the analysis of a sample of GUF-12(Hf) subjected to bromination conditions will be provided as a guide. Typically, full conversion of the EDB²⁻ linker to EDB-Br₂²⁻ was observed, which can be seen by the increased separation of the resonances assigned to the aromatic ligand protons when comparing ¹H NMR spectra (Figure S21). As with bromination of the **fcu** derivatives, stereoselective *trans* debromination occurred exclusively due to the mechanical constraints imposed upon the EDB²⁻ ligand when part of the MOF network.

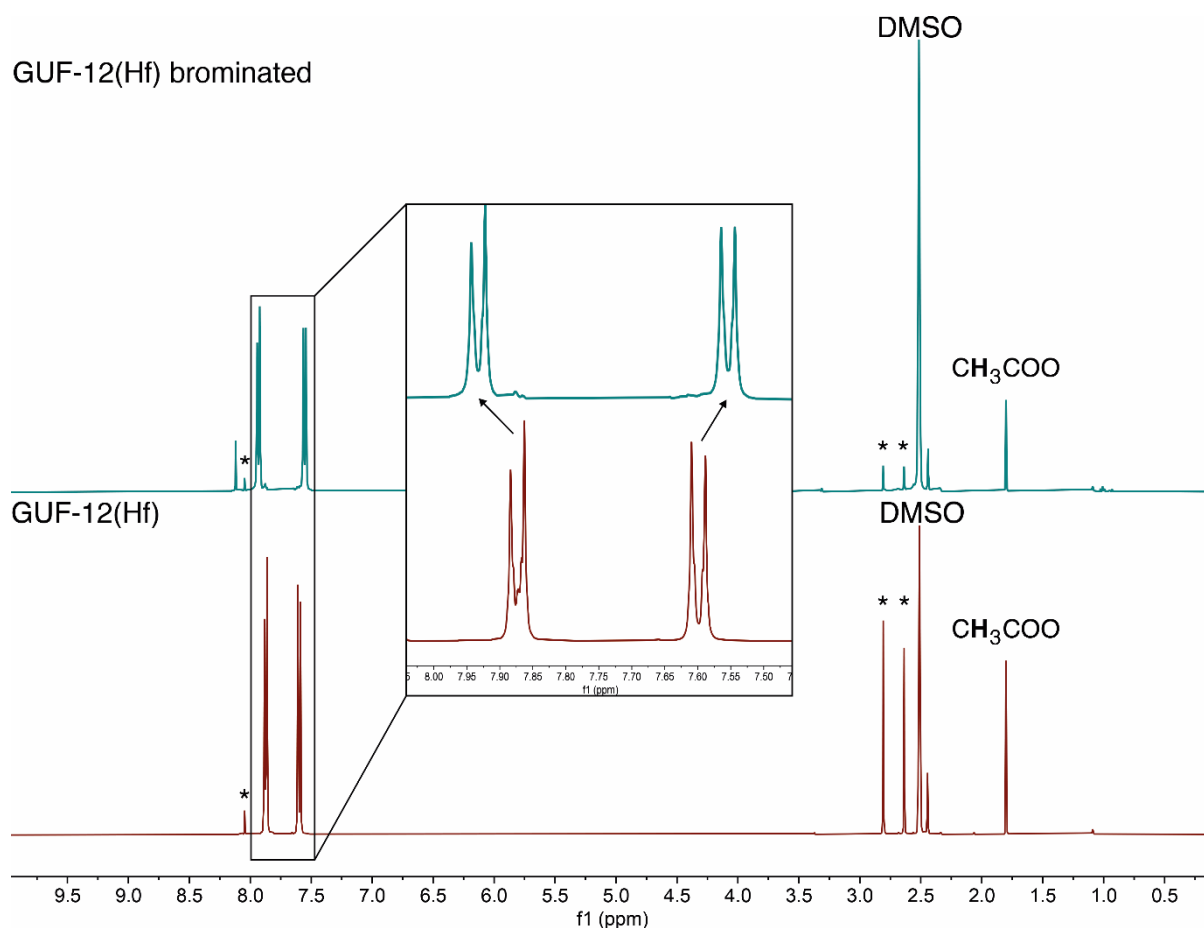


Figure S21. Stacked partial NMR spectra (DMSO- d_6 / D $_2$ SO $_4$) of GUF-12(Hf) before and after bromination. The inset provides a close up view of the resonances assigned to the aromatic protons of the linkers, which become more separated upon bromination of the alkyne unit. The resonances marked with an asterisk (*) at $\delta = 2.6, 2.8,$ and 8 ppm are assigned to DMF protons. These were present in varying ratios across samples (including increasing after activation) suggesting that they are a contaminant in the NMR tubes.

The stability of the **hcp** phase MOFs to bromination was problematic; PXRD analysis of the bromination of GUF-12(Hf) is representative of the results in general (Figure S22). The fact that a change in the relative intensities of the two most intense reflections of the hcp phase (100) and (101) occurs suggests possible partial delamination of the GUF-12(Hf), which has previously been observed by physical stimulus in an isorecticular analogue.^{S17} If this is the case, some obtainment of residual ligand, from the disruption of *c*-direction stacking, could explain the additional reflections around $2\theta \sim 20-30^\circ$, but further work would be required to establish this.

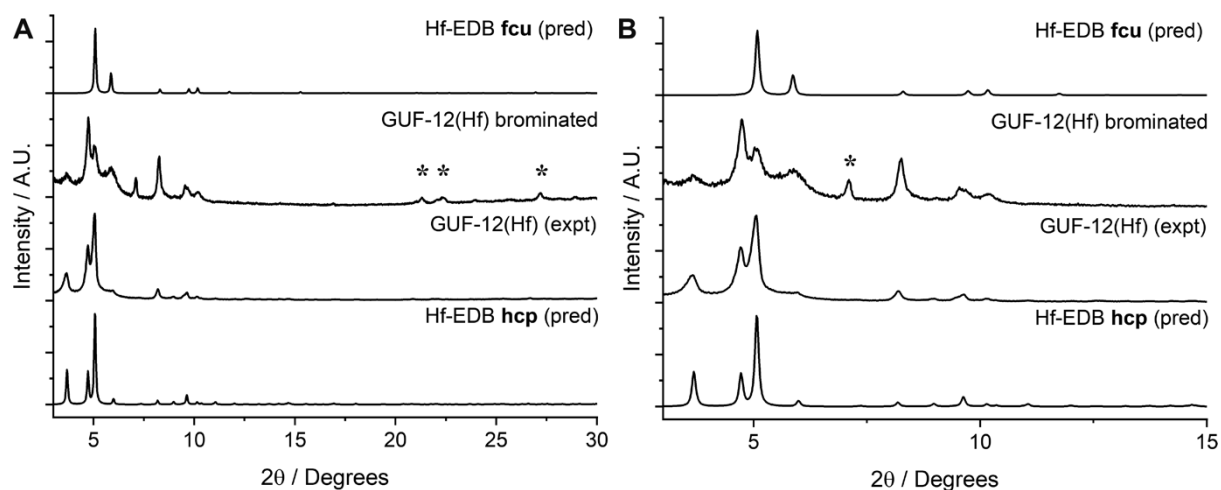


Figure S22. Stacked powder X-ray diffractograms of GUF-12(Hf) before and after bromination compared with predicted patterns for the **hcp** phase MOFs derived from DFT models (see Section S3) and the **fcu** phase MOFs derived from their crystal structures.^{S1} In part (A), reflections marked with an asterisk (*) are thought to correspond to free ligand, suggestive of MOF decomposition. In the expansion in part (B), an additional reflection marked with an asterisk (*) at $2\theta \sim 7^\circ$ is further indicative of structural change, as are the changes in relative intensities and broadening of the main Bragg reflections.

S9. References

- S1. R. J. Marshall, S. L. Griffin, C. Wilson and R. S. Forgan, *J. Am. Chem. Soc.*, 2015, **137**, 9527-9530.
- S2. T. Gadzikwa, B.-S. Zeng, J. T. Hupp and S. T. Nguyen, *Chem. Commun.*, 2008, 3672-3674.
- S3. F. C. N. Firth, M. J. Cliffe, D. Vulpe, M. Aragonés-Anglada, P. Z. Moghadam, D. Fairen-Jimenez, B. Slater and C. P. Grey, *J. Mater. Chem. A*, 2019, **7**, 7459-7469.
- S4. J. VandeVondele, M. Krack, F. Mohamed, M. Parrinello, T. Chassaing and J. Hutter, *Comp. Phys. Commun.*, 2005, **167**, 103-128.
- S5. J. Hutter, M. Iannuzzi, F. Schiffmann and J. VandeVondele, *Wiley Interdiscip. Rev. Comput. Mol. Sci.*, 2014, **4**, 15-25.
- S6. J. VandeVondele and J. Hutter, *J. Chem. Phys.*, 2007, **127**, 114105.
- S7. S. Goedecker, M. Teter and J. Hutter, *Phys. Rev. B*, 1996, **54**, 1703-1710.
- S8. M. Krack, *Theor. Chem. Acc.*, 2005, **114**, 145-152.
- S9. J. P. Perdew, K. Burke and M. Ernzerhof, *Phys. Rev. Lett.*, 1996, **77**, 3865-3868.
- S10. S. Grimme, J. Antony, S. Ehrlich and H. Krieg, *J. Chem. Phys.*, 2010, **132**, 154104.
- S11. A. A. Coelho, J. Evans, I. Evans, A. Kern and S. Parsons, *Powder Diffr.*, 2011, **26**, S22-S25.
- S12. J. W. M. Osterrieth, J. Rampersad, D. Madden, N. Rampal, L. Skoric, B. Connolly, M. D. Allendorf, V. Stavila, J. L. Snider, R. Ameloot, J. Marreiros, C. Ania, D. Azevedo, E. Vilarrasa-Garcia, B. F. Santos, X.-H. Bu, Z. Chang, H. Bunzen, N. R. Champness, S. L. Griffin, B. Chen, R.-B. Lin, B. Coasne, S. Cohen, J. C. Moreton, Y. J. Colón, L. Chen, R. Clowes, F.-X. Coudert, Y. Cui, B. Hou, D. M. D'Alessandro, P. W. Doheny, M. Dincă, C. Sun, C. Doonan, M. T. Huxley, J. D. Evans, P. Falcaro, R. Ricco, O. Farha, K. B. Idrees, T. Islamoglu, P. Feng, H. Yang, R. S. Forgan, D. Bara, S. Furukawa, E. Sanchez, J. Gascon, S. Telalović, S. K. Ghosh, S. Mukherjee, M. R. Hill, M. M. Sadiq, P. Horcajada, P. Salcedo-Abraira, K. Kaneko, R. Kukobat, J. Kevlin, S. Keskin, S. Kitagawa, K.-i. Otake, R. P. Lively, S. J. A. DeWitt, P. Llewellyn, B. V. Lotsch, S. T. Emmerling, A. M. Pütz, C. Martí-Gastaldo, N. M. Padial, J. García-Martínez, N. Linares, D. MasPOCH, J. A. Suárez del Pino, P. Moghadam, R. Oktavian, R. E. Morris, P. S. Wheatley, J. Navarro, C. Petit, D. Danaci, M. J. Rosseinsky, A. P. Katsoulidis, M. Schröder, X. Han, S. Yang, C. Serre, G. Mouchaham, D. S. Sholl, R.

- Thyagarajan, D. Siderius, R. Q. Snurr, R. B. Goncalves, S. Telfer, S. J. Lee, V. P. Ting, J. L. Rowlandson, T. Uemura, T. Iiyuka, M. A. van der Veen, D. Rega, V. Van Speybroeck, S. M. J. Rogge, A. Lamaire, K. S. Walton, L. W. Bingel, S. Wuttke, J. Andreo, O. Yaghi, B. Zhang, C. T. Yavuz, T. S. Nguyen, F. Zamora, C. Montoro, H. Zhou, A. Kirchon and D. Fairen-Jimenez, *Adv. Mater.*, 2022, **34**, 2201502.
- S13. D. Dubbeldam, S. Calero, D. E. Ellis and R. Q. Snurr, *Mol. Simul.*, 2016, **42**, 81-101.
- S14. S. L. Mayo, B. D. Olafson and W. A. Goddard, *J. Phys. Chem.*, 1990, **94**, 8897-8909.
- S15. A. K. Rappe, C. J. Casewit, K. S. Colwell, W. A. Goddard, III and W. M. Skiff, *J. Am. Chem. Soc.*, 1992, **114**, 10024-10035.
- S16. J. J. Potoff and J. I. Siepmann, *AIChE J.*, 2001, **47**, 1676-1682.
- S17. M. J. Cliffe, E. Castillo-Martínez, Y. Wu, J. Lee, A. C. Forse, F. C. N. Firth, P. Z. Moghadam, D. Fairen-Jimenez, M. W. Gaultois, J. A. Hill, O. V. Magdysyuk, B. Slater, A. L. Goodwin and C. P. Grey, *J. Am. Chem. Soc.*, 2017, **139**, 5397-5404.